Uncertainty Quantification in Tomographic Inversion of Near-Surface Seismic Refraction Data

Ang Li[1] · **Dario Grana[1]** · **Andrew D. Parsekian[1,2]** · **Brad Carr[1]**

Abstract

Understanding the near-surface structure of the Earth requires accurate prediction of physical properties of the subsurface, such as velocity estimated from tomographic inversion of seismic refraction data. The predicted velocity values are often uncertain due to epistemic uncertainty in the inversion process (i.e., imperfectly known underlying physics) and aleatoric variability in the data (i.e., inherent noise in observations). Although seismic refraction is widely used in near-surface applications, the associated uncertainty is rarely quantified and presented alongside the inverted velocity tomograms. In this study, the effect of epistemic uncertainty due to local variability in the initial model and aleatoric variability due to first-arrival picking error on the velocity prediction uncertainty are investigated. A stochastic framework is implemented based on a statistical approach where multiple realizations of stochastically perturbed initial models and travel time picks are generated and the uncertainty in the predicted velocity models is quantified. The two sources of uncertainty are first studied independently and then the combined effect is investigated. The results show that both sources affect the posterior uncertainty, but the uncertainty in the initial model has a greater effect than picking error on the uncertainty of the posterior velocity model. In addition, joint analysis of both sources of uncertainty shows that the uncertainty in the inverted model depends on predicted velocity values, depths, velocity gradients and ray coverages.

Keywords Seismic refraction · Seismic inversion · Stochastic methods · Uncertainty quantification · Rock properties · Near-surface geophysics

✉ Ang Li
ali@uwyo.edu

1 Department of Geology and Geophysics, University of Wyoming, Laramie, WY, USA

2 Department of Civil, Architectural Engineering and Construction Management, University of Wyoming, Laramie, WY, USA

🖄 Springer

1 Introduction

The top tens-of-meters below the Earth's surface play a central role in the processes that sustain life on Earth (Anderson et al. 2005; Brantley et al. 2007; Leopold et al. 2013; Moravec et al. 2020; Riebe et al. 2017). For example, subsurface weathering opens pore spaces and breaks down minerals, which facilitates storage and through-flow of groundwater and soil nutrients (White et al. 2019; Hahm et al. 2019; Bales and Dietrich 2020; McCormick et al. 2021; Callahan et al. 2022). Because of the high heterogeneity in the near-surface, understanding the controls on hydrological dynamics and subsurface structure often relies on estimating material properties (Knight and Endres 2005; Moysey et al. 2005; Singha and Moysey 2006; Robinson et al. 2008) such as porosity and saprolite thickness (Holbrook et al. 2014; Prakoso et al. 2018; Gase et al. 2018; Flinchum et al. 2018a, 2022; Hayes et al. 2019; Callahan et al. 2020; Gu et al. 2020; Grana et al. 2022) and depth of the bedrock (St. Clair et al. 2015; Flinchum et al. 2018b; Rempe and Dietrich 2018; Holbrook et al. 2019; Ackerer et al. 2020). Well-logging (Holbrook et al. 2019) and core sampling (Hayes et al. 2019; Riebe et al. 2021) are often used to provide direct measurements of subsurface rock properties as a function of depth with increased accuracy and resolution. However, these direct measurements are sparsely sampled at a limited number of locations where boreholes are available. Instead, near-surface geophysical imaging, for example seismic refraction tomography, is an effective technique for providing spatially continuous imaging of the subsurface and is more representative of the near-surface structure at a larger scale than direct digging or boring (Befus et al. 2011; Parsekian et al. 2015). While shallow seismic refraction methods have been widely used, investigation of uncertainties of these datasets is limited (e.g., Holbrook et al. 2014; Parsekian et al. 2021; Marciniak et al. 2019). In these cases, the calculated uncertainties are used to illustrate the accuracy of the velocity model, but the effect of the different sources of error on the calculated uncertainties is not addressed. To make reliable predictions of subsurface parameters based on interpretation of seismic velocity, uncertainty in the inverted seismic velocity tomogram needs to be quantified. This study focuses on the uncertainty effects of two factors on the inverted seismic velocity tomogram: local variations in the initial model used for inversion and errors in the travel time picking process.

In geophysical inverse problems, several methods are developed to quantify the uncertainty of the model variables of interest based on the uncertainty in the data and the uncertainty in the physical relations between model and data (Borcherdt and Healy 1968; Tarantola 2005; Aster et al. 2018). For example, bootstrap resampling (Efron 1979, 1982) has been used to quantify the variability in inverse solutions for various geophysical methods (Rawlinson et al. 2014; Schnaidt and Heinson 2015). Bootstrapping is based on randomly resampling a population of smaller size than the original dataset, inverting the resampled population, creating multiple solutions, and computing the statistical properties of interest on the ensemble of inverted models. Alternatively, probabilistic approaches such as Bayesian methods have also been proposed (Tarantola 2005). For example, Gouveia and Scales (1998) used Bayesian statistics to combine a probability distribution based on a priori information and a likelihood function into the posterior distribution of the model variable, which provides a

quantification of the model uncertainty. As the physical relations between model and data are non-linear and the posterior distribution is generally represented by a complex probability density function, stochastic methods such as Markov chain Monte Carlo algorithms are adopted. In these methods, a proposed model is randomly sampled and accepted or rejected based on data fit, and the posterior distribution is estimated from the ensemble of accepted models whose variance represents the uncertainty in the ensemble (Liu and Stock 1993; Chen et al. 2010; Huang et al. 2021).

Sources of uncertainty in the tomographic inversion of shallow seismic refraction data include aleatoric uncertainty that is associated with randomness in the measured data and epistemic uncertainty that is related to lack of prior knowledge of the physical model (Palmer 2012). With respect to the latter, Palmer (2012) first proposed the hypothesis that minimizing the epistemic uncertainty with an accurate initial model is more effective than minimizing data error for shallow seismic refraction data. Because of the non-uniqueness of the solution of tomographic inverse problems, building physically plausible initial models is crucial. Indeed, without a physically plausible initial model, many inversion algorithms might fail (Chen and Zelt 2016; Cai and Zelt 2022). In other studies, uncertainty in the inverted seismic result was investigated by studying the sensitivity of using a range of velocity gradients to update the initial model (Holbrook et al. 2014).

Aleatoric uncertainty in seismic refraction data often arises from measurement acquisition and data processing and manipulation (Rawlinson et al. 2014). Generally, measurement errors decrease signal to noise ratio and propagate into data processing error (e.g., arrival time picking). Dangeard et al. (2018) proposed a method to estimate picking error for shallow seismic refraction data by repeating the waveform picking multiple times and found median picking uncertainties were less than 1%. Uncertainty in travel time data is frequently quantified using the reciprocity principle (DeHoop 1966), which states that reciprocal travel time recordings, where the source and receiver positions are interchanged, are expected to be identical in viscoelastic media. Therefore, the mismatch for reciprocal data with respect to the identity function approximates the uncertainty in the travel time data. However, in most seismic refraction surveys, it is impractical to generate a seismic source at every sensor location to obtain a complete set of reciprocal data. Hence, in cases where reciprocal traces are missing, interpolation is used or a constant uncertainty equal to the root-mean-squared amplitude of all the computable reciprocal errors is used (Zelt and Chen 2016; Cai and Zelt 2022). Alternatively, statistical models based on least-squares optimization have been used to quantify uncertainty in travel time data (Steinhart and Meyer 1961). However, it has not been shown in previous studies how data uncertainty affects the uncertainty in the inverted velocity model.

In this study, a linear velocity trend is assumed in the initial model between the surface and bedrock (following Holbrook et al. 2014); however, lateral variability in the initial model is introduced to study the effect on the inverted models. The uncertainty in the velocity model is quantified, and the effect of the picking uncertainty is investigated using a stochastic framework. The objectives herein are as follows: (i) to demonstrate a stochastic approach to quantify the uncertainty in the inverted velocity model, and (ii) to investigate the variability in velocity model predictions due to different sources of error. This work addresses the open scientific question: how do

input errors (i.e., uncertainty in the initial model and in the data) drive uncertainty in the inverted tomographic velocity models? The methodology is demonstrated on a field-measured seismic refraction dataset from the Laramie Range, Wyoming, USA. The structure of the paper is as follows: The Methods section presents the field data acquisition, reviews the tomographic inversion, and defines a stochastic framework of perturbing the initial model and data for quantification of the uncertainty in the posterior velocity model. The Application section applies the proposed methodology to seismic refraction field data to study the effect of increasing variability in inversion inputs on the inverted velocity models, and the Discussion section presents advantages and limitations of the proposed method and broader implications of uncertainty quantification in seismic inversion for near-surface geophysical studies.

2 Methods

This section describes field data acquisition and inversion. Inversion results are studied to quantify the variability in model predictions that depends on the uncertainty in measured data and initial model assumptions.

2.1 Field Data Acquisition

Seismic refraction is a geophysical technique that measures the travel times of active-source seismic waves propagating in the subsurface using receivers. The receivers (i.e., geophones) record the amplitudes and arrival times of the refracted signal turned back towards the surface due to contrasts in density and bulk modulus. In this work, the focus is on first arrivals recorded in seismograms.

Seismic refraction datasets were collected along two transects near Pilot Peak (PP) and two transects near Government Gulch (GG), both in the Laramie Range, Wyoming, USA, in July 2022 (Fig. 1a). The geological substrate is a layered sedimentary sequence including the Casper Formation, which comprises permeable sandstones and less permeable interbedded limestones, resting on top of Precambrian crystalline rocks (Huntoon and Lundy 1979). Two intersecting 110-m-long transects from each site that run approximately north–south (PP8 and GG3) and east–west (PP10 and GG4) were selected for this study (Fig. 1b, c). To collect seismic refraction data, two 24-channel Geometrics Geode systems with 48 10-Hz vertical component geophones at 2-m spacing were used. The seismic energy was generated by striking a 5.4 kg sledgehammer on a 20 cm × 20 cm × 1 cm steel plate at 10-m intervals along each transect, with eight stacks at each shot location. Relative elevation along each transect was obtained using hand sight level survey at 2-m spacing.

Seismic data were picked using the Geogiga Seismic Pro DW Tomo module (Geogiga Software, Calgary, Canada). First-arrival travel times were manually picked by the same operator for every trace in the waveform data. A few geophone channels suffered from low quality recording; hence, the associated traces were discarded for visualization purposes (Fig. 2). No band-pass filter was used before or during the picking process.
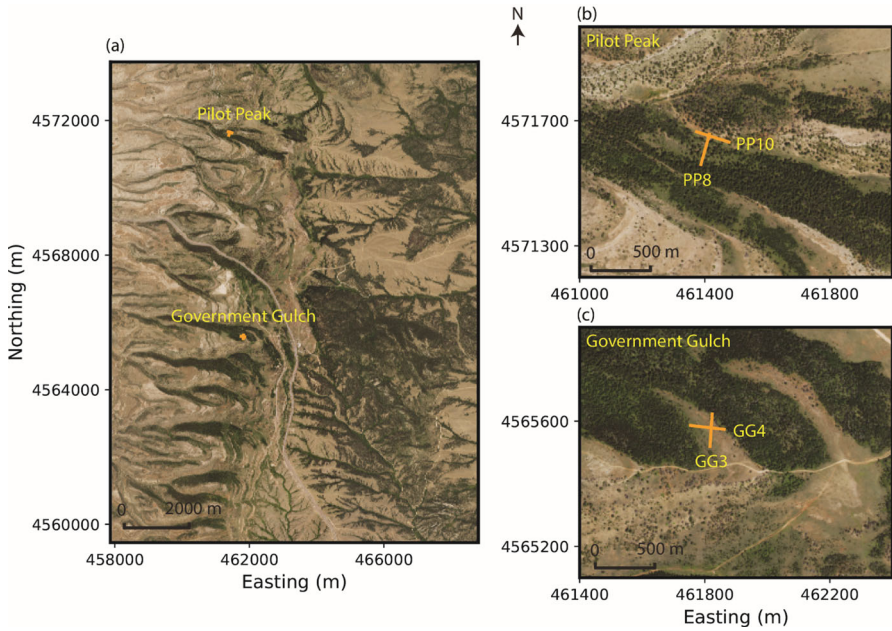
Fig. 1 Field site at Pilot Peak (PP) and Government Gulch (GG) near Laramie, Wyoming (**a**). Seismic refraction transects PP8 and PP10 at Pilot Peak (**b**), GG3 and GG4 at Government Gulch (**c**)
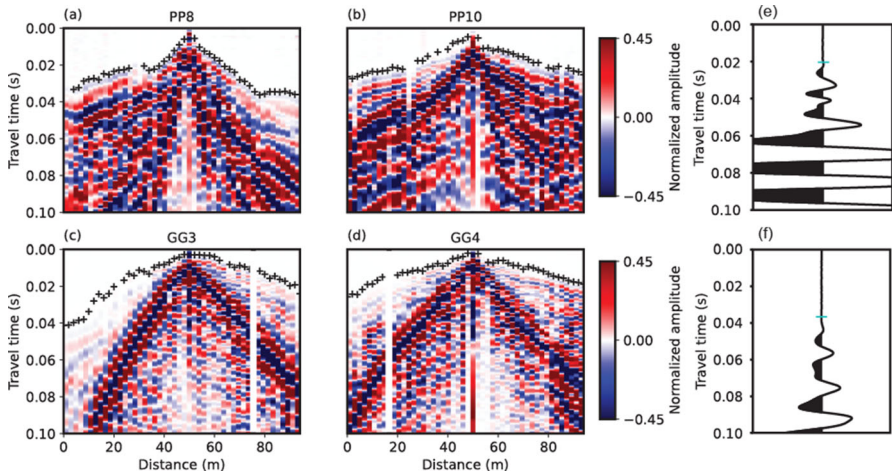

Fig. 2 Normalized seismic waveform data for a seismic source location at 50 m for PP8 (**a**), PP10 (**b**), GG3 (**c**) and GG4 (**d**) (first-arrival picks are shown as black crosses), and two seismic traces (**e, f**) extracted from PP10 data at 80 m and from GG3 data at 8 m, respectively, with first-arrival picks shown in blue

2.2 Tomographic Inversion

First-arrival picks were tomographically inverted to obtain two-dimensional images of compressional wave velocities (e.g., P-wave velocities) in the subsurface. Travel-time tomography inversion is an underdetermined problem where the number of unknowns is larger than the number of measurements (Tarantola 2005). Therefore, the solution is non-unique. For the data presented in this study, the inversion was done using the Python Geophysical Inversion Modeling Library (PyGIMLi) (Rücker et al. 2017).

The seismic tomographic problem can be written as a function $f : \mathbb{R}^M \to \mathbb{R}^N$ that approximates the physical relation between the velocity model m (vector of length M) and picked travel time data d (vector of length N) as

$$d = f(m) + \varepsilon, \tag{1}$$

with measurement error ε (vector of length N). Hence, the inverse problem aims at determining the velocity model $\hat{m}$ that minimizes the misfit between data predictions and data measurements

$$\hat{m} = \operatorname{argmin} f(m) - d. \tag{2}$$

The solution to the tomographic inverse problem is generally computed as an optimization process where an initial model is proposed, and it is updated to minimize the mismatch of the measured data (travel times) and model predictions. The optimization is performed using deterministic or stochastic methods. The inversion framework in PyGIMLi is based on a deterministic Gauss–Newton scheme that minimizes an objective function $g(m)$ that contains the data misfit and a regularization term (Rücker et al. 2017)

$$g(m) = \|W_d(f(m) - d)\|_2^2 + \lambda \|W_m(m - m_0)\|_2^2, \tag{3}$$

where d ($M \times 1$) is the vector of travel times, with N being equal to the product of the number of sources times the number of receivers, m ($M \times 1$) is the velocity model of interest, with M being the number of locations with unknown velocity values, and m_0 ($M \times 1$) is the initial velocity model. The matrix W_d ($N \times N$) is the data weighting matrix that contains data errors used to weight travel time picks in the inversion such that travel times with the smallest errors are given the most weight. Flinchum et al. (2022) assigned errors to travel time picks using a linear equation as a function of offset distance from the source. Alternatively, a constant error value is assigned to data so that all travel times are given with equal weight. The matrix W_m ($M \times M$) is the model constraint matrix, also known as a first-order smoothness operator, whereas the dimensionless factor λ is a regularization term, also referred to as smoothing scalar.

The function f calculates travel times of the subsurface model with velocity model m using Dijkstra's shortest path algorithm (Dijkstra 1959). The algorithm uses an iterative method to find the shortest path between a source node and a set of other nodes, for which it updates the shortest distance between each node to the source node until all nodes are added to the path. The geometric domain where the velocity model

is defined is a triangular mesh is used to improve numerical accuracy and minimize mesh interpolation errors (Rücker et al. 2017).

The following inversion settings are used in this study: a value of 200 is used as the smoothing scalar λ for the regularization term and a maximum number of 15 iterations is allowed for the inversion to converge. Inversion is also constrained by limiting the velocity range to be between 300 and 6,000 m/s to avoid predicting physically implausible velocity values. The depth of investigation (DOI) is defined as the maximum depth where the inversion results are considered reliable, and it depends on the acquisition geometry and on the actual velocity structure of the subsurface. The DOI is bounded by the deepest calculated ray path on the velocity tomogram.

2.3 Uncertainty Quantification

To investigate the uncertainty in the inverted velocity model, a Monte Carlo approach is adopted, where the inversion is run multiple times by minimizing the objective function $g(\boldsymbol{m})$ with different initial conditions and data errors. The initial model is created by defining a top layer with low velocity that represents soil with high porosity and a bottom layer with higher velocity that represents local bedrock. The velocity structure is linearly interpolated following the surface topography. The maximum depth of the parametric domain is set as 60 m based on the analysis of the modeled ray path geometry. The number of equidistant nodes between two geophones is set to 3. The maximum parametric size for triangles is set to 3 m^2.

Since the model is defined on a triangular grid, the application of traditional geostatistics methods to stochastically generate the set of initial models is challenging. For this reason, a deterministic initial model is first defined according to a linear depth trend of velocity and a spatially correlated random noise is added to the model. To generate a set of spatially correlated models, spatially uncorrelated random noise is added to a subset of randomly selected locations within the grid and then the values are interpolated to obtain locally continuous models. The random noise is drawn from a uniform distribution with a pre-defined variance. The local continuity of the initial models depends on the number of subsampled points (i.e., subsample size) and the noise variance. If the subsample size is too large, the stochastic models show abrupt local variations, whereas if the subsample size is too small, the overall variability is relatively limited. A similar argument can be made for the variance of the noise. After performing a sensitivity analysis on the effect of variation in subsample size, a subsample size of 500 (approximately 20% of the total number of points in the grid) was chosen. According to a Monte Carlo approach, the inversion was run n times with an ensemble of n stochastically perturbed initial models. The solution is an ensemble of n realizations whose mean represents the most likely P-wave velocity model, and the standard deviation is interpreted as the uncertainty of the P-wave velocity model due to the uncertainty in the prior knowledge and the data processing error. The mean μ_m and standard deviation σ_m are computed from the posterior ensemble of realizations at each point of the model grid.

The uncertainty due to data picking errors is investigated by simulating random errors to be added to the picked travel times. For this study, a random error with a

Gaussian distribution $N\left(\mu_e, \sigma_e^2\right)$ is assumed with mean μ_e equal to zero. Because the signal-to-noise ratio of the data generally decreases with distance from the seismic source location as the first-arrival times increase, the standard deviation of the error is assumed to be a function of first-arrival travel times. Therefore, the standard deviation is locally variable and is defined such that the half-length of the 0.95 confidence internal $(1.96\sigma_e)$ is equal to a fraction of the travel time ϵt_p, with $\epsilon < 1$. Consequently, the standard deviation of picking error σ is assumed to be $(\epsilon/1.96)t_p$ and the perturbed travel time t_p^* is

$$t_p^* = t_p + z, \quad \text{with } z \sim N\left(0, \sigma_e^2\right), \tag{4}$$

where t_p denotes the picked travel time. The inversion is run n times with n perturbed travel time datasets, and the solution is an ensemble of n realizations used to predict the mean μ_m and standard deviation σ_m that represent the most likely P-wave velocity model and uncertainty in the P-wave velocity model.

It is certainly difficult to correctly define the uncertainty in the initial conditions and data; however, based on literature data and direct measurements, it is possible to define plausible ranges for their variability. In this study, three different cases are considered for the uncertainty in the initial model, representing the low-uncertainty, mid-uncertainty and high-uncertainty cases to study the effect on the posterior model mean and standard deviation. The uncertainty in the initial model depends on the standard deviation of the local errors that control the variability in the set of initial models. Similarly, three different cases are considered for the uncertainty in the data picks, representing the low-uncertainty, mid-uncertainty and high-uncertainty cases. The uncertainty in the picking errors depends on the standard deviation of the data error that controls the variability in the travel times. The two sources of uncertainty for the velocity model are first studied independently; in other words, the uncertainty due to the variability in the initial model is investigated assuming no picking error in the data, and the uncertainty due to the picking error is investigated with the same initial model. Then, the uncertainty in the velocity model due to the initial model and the picking error is studied by simultaneously perturbing the initial model and travel time data.

3 Application

Seismic data are first inverted using the standard pyGLIMLi inversion for all four transects; then the stochastic approach is applied to investigate the variability in the P-wave velocity model due to the uncertainty in the initial model and the picking error. The result of the traditional inversion is a single P-wave velocity model for each transect. For plotting the inverted velocity tomograms, perceptually uniform colormaps (Crameri 2021) are used. Figure 3b shows the inverted P-wave velocity tomogram for transect PP8 with a root-mean-squared-error (RMSE) misfit of 1.27 ms after four iterations. Transect PP8 is a 110-m-long line that starts at a north flat ridgetop, drops into a topographic minimum at approximately 30 m on a hillslope, then rises up to
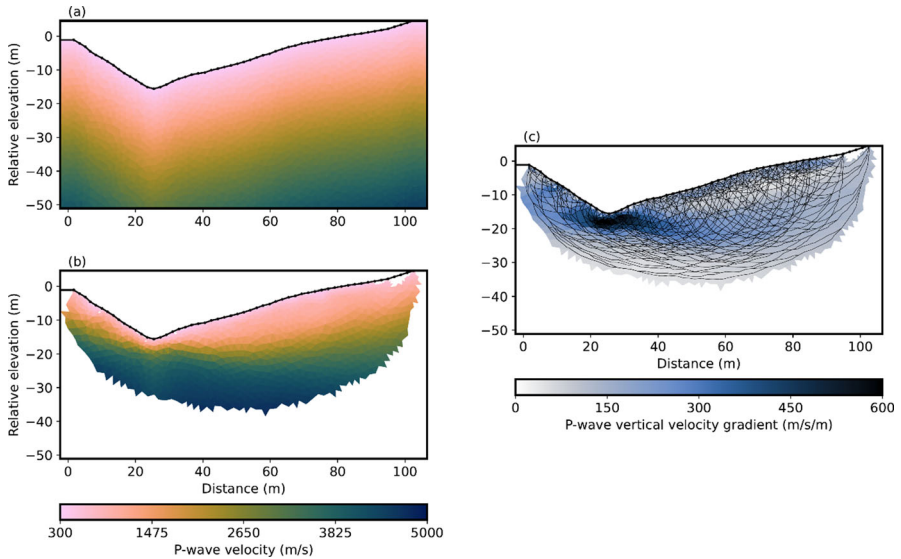
Fig. 3 Initial model (**a**) and inversion result for PP8: P-wave velocity model (**b**), calculated vertical velocity gradient and ray path (**c**) (ray path thicknesses are used for visualization). Black dots represent geophone locations along the hillslope

a south flat ridgetop. The inverted model is only plotted above the DOI based on the deepest ray path (Fig. 3b). The vertical velocity gradient is calculated in the model, and darker colors indicate areas with a sharp vertical increase in velocity (Fig. 3c). Regions with high vertical velocity gradient values are commonly associated with lithological boundaries. In Fig. 3b, two distinguishable layers with different velocity values and thicknesses are identified: (i) a low-velocity layer ($V_p < 1,000$ m/s) that is interpreted as unconsolidated rocks, and (ii) a high-velocity layer ($V_p > 3,000$ m/s) that is interpreted as consolidated rocks. This velocity contrast may be associated with porosity and lithology changes (Flinchum et al. 2018b). The calculated vertical velocity gradient is the highest under the topographic low point at 30 m and highlights the transition zone of low-velocity layer to high-velocity layer (Fig. 3c).

3.1 Uncertainty in the Initial Model

In this section, the uncertainty due to the initial velocity model is investigated. A set of 100 realizations of initial velocity model is generated and for each initial model the inversion is run. The result is a set of 100 posterior velocity models conditioned on the seismic data from which the velocity uncertainty can be estimated. The mean of 100 realizations of initial velocity model is calculated for the three cases of uncertainties (Fig. 4a–c). One realization is randomly selected to illustrate the local perturbation added to the initial model (Fig. 4d–f). The standard deviation that represents the variability in the prior ensemble of 100 realizations for the three cases of uncertainties is calculated (Fig. 4g–i). For the low-uncertainty case scenario, the feature of a smooth
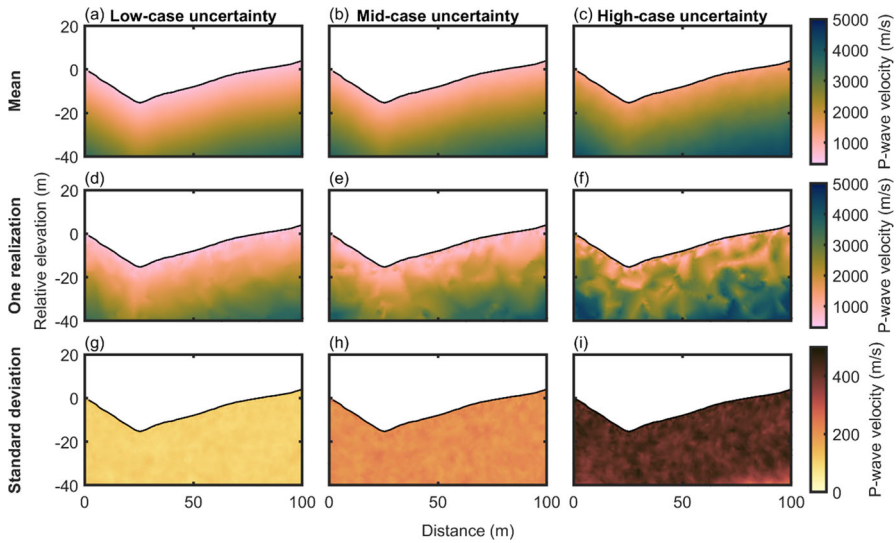
Fig. 4 Initial model of P-wave velocity for PP8: mean of 100 realizations (**a–c**), one randomly selected realization (**d–f**), and standard deviation of 100 realizations (**g–i**) obtained by perturbing the initial model at low-, mid- and high-uncertainty cases

and linear gradient initial model is still preserved (Fig. 4a, d). At mid-uncertainty and high-uncertainty case scenarios, structure of the initial model becomes more variable and less smooth (Fig. 4b, c, e, f). As a result of subsampling and interpolation, the perturbed model is still locally continuous (Fig. 4g–i).

Using a Monte Carlo approach, the inversion is run 100 times with the stochastically perturbed initial models. The mean of the ensemble of posterior realizations is assumed to be the most likely P-wave velocity model (Fig. 5a–c). By comparing to the result obtained using a deterministic approach (Fig. 3b), it is clear that the most likely model preserves similar structural patterns of velocity across all three cases of uncertainties. However, for a randomly selected realization, the posterior velocity model appears to be less spatially continuous as variability in the set of initial models increases (Fig. 5d–f). The standard deviation of posterior velocity models decreases with respect of the initial standard deviation in each case. However, the variability in the posterior ensemble of realizations increases as variability in the set of initial models increases from the low-uncertainty to the high-uncertainty case (Fig. 5g–i).

To quantitatively illustrate the effect of initial model uncertainty on the posterior model variability, box plots for the initial model ensemble and the posterior model ensemble are shown (Fig. 6). For the three cases of uncertainties, the inversion converges to approximately the same distribution of the mean of the posterior ensemble of realizations (Fig. 6b), whereas the standard deviation shows that the median and the interquartile range increase as the variability in the set of initial models increases (Fig. 6d).
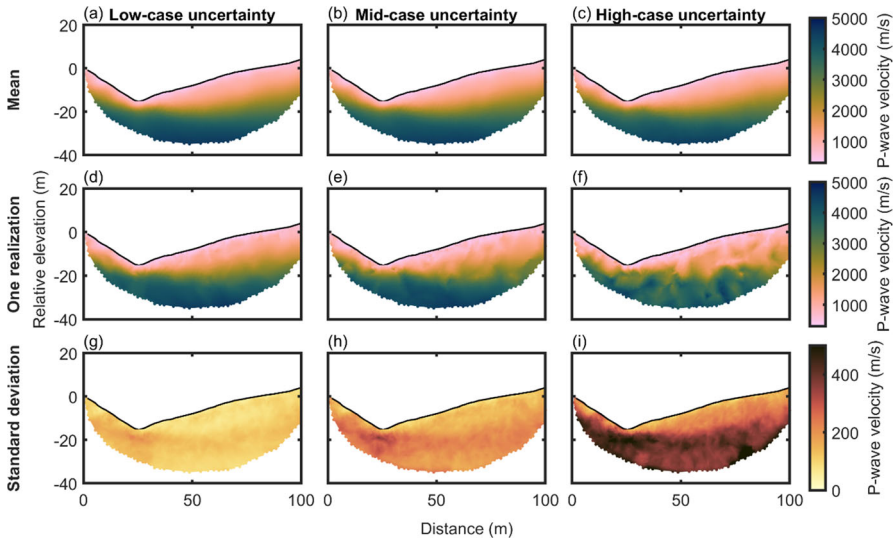
Fig. 5 Posterior model of P-wave velocity for PP8: mean of 100 realizations (**a–c**), one randomly selected realization (**d–f**), and standard deviation of 100 realizations (**g–i**) obtained by perturbing the initial model at low-, mid- and high-uncertainty cases

3.2 Uncertainty in the Data

In this section, the uncertainty in the picking arrival times is studied, by defining the picking error as a fraction of the measured travel time of the interpreted first arrival. Three different cases representing the low-uncertainty, mid-uncertainty and high-uncertainty cases are investigated to stochastically perturb the travel time data. Reciprocal data of original picks (Fig. 7a) and reciprocal data of the ensemble of 100 realizations of perturbed travel time picks at the mid-uncertainty case (Fig. 7b, c) illustrate the variability in the perturbed data and shows that the perturbed data are still within a physically plausible range. Picking errors for travel time picks at each trace are shown with error bars (Fig. 8a–c). For each case of uncertainty, stochastically perturbed travel time data are used as input for the inversion and the posterior P-wave velocity model is obtained. Using a Monte Carlo approach, inversion is run 100 times using 100 stochastically perturbed travel time data points. The mean of the ensemble of posterior realizations represents the most likely P-wave velocity model (Fig. 9a–c). The mean for the three cases of uncertainty shows similar velocity structure. One realization is randomly selected to show the effect of picking error on the inverted model (Fig. 9d–f). The standard deviation of posterior velocity models shows that variability in the posterior ensemble of realizations increases as picking error increases (Fig. 9g–i). For the three cases of uncertainty, the inversion converges to the same distribution of the mean of the posterior ensemble of realizations (Fig. 8d), whereas the median and the interquartile range of the standard deviation increase as picking error increases (Fig. 8e). In other words, even though the standard deviation
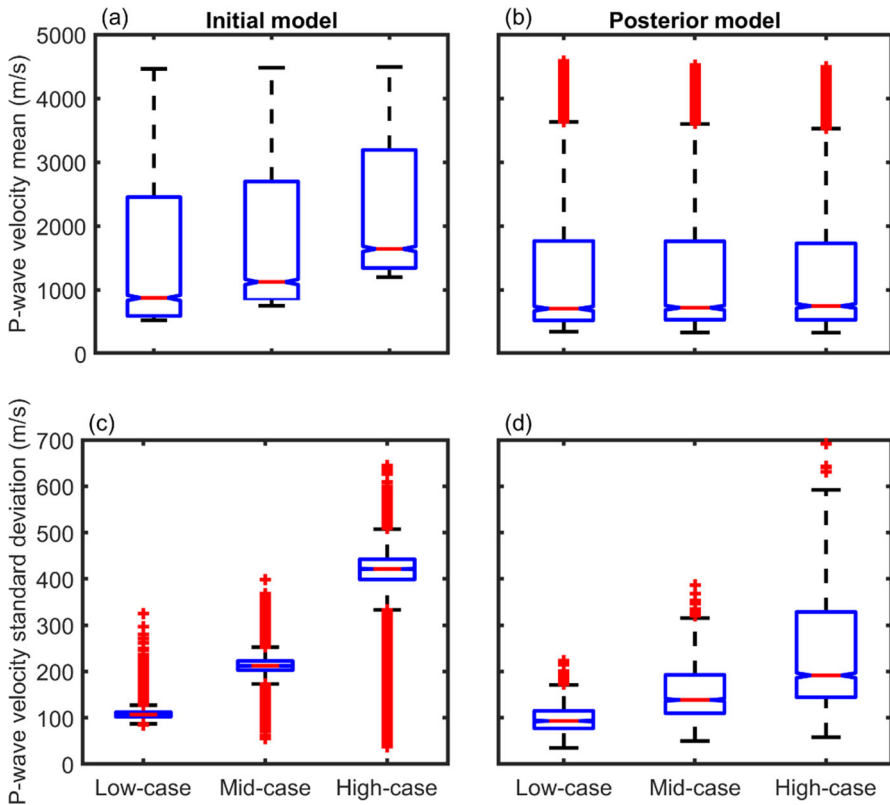
Fig. 6 Box plots of mean (**a**) and standard deviation (**c**) for initial model and box plots of mean (**b**) and standard deviation (**d**) for posterior model obtained by perturbing the initial model

of the posterior velocity model increases, the inversion results converge to a consistent posterior velocity despite the increasing magnitude of the error.

To compare the independent effect of initial model uncertainty and picking error on the variability in the posterior ensemble, differences in the ensemble mean within three cases of uncertainties are calculated from previously shown results obtained by perturbing the initial model (Fig. 5a–c) and picking data (Fig. 9a–c). The calculated differences in the ensemble mean of the low- and mid-uncertainty scenarios (Fig. 10a, c) and of the low- and high-uncertainty scenarios (Fig. 10b, d) show that the posterior ensemble mean becomes more locally variable as initial model uncertainty and picking error increase and that the difference in the ensemble mean obtained in case of initial model uncertainty (Fig. 10a, b) is generally higher than difference obtained in case of picking error (Fig. 10c, d). Overall, the conclusions herein are as follows: (i) both initial model uncertainty and picking error drive uncertainty in the posterior velocity model; (ii) initial model uncertainty has a larger effect on the variability in the posterior model than picking error.
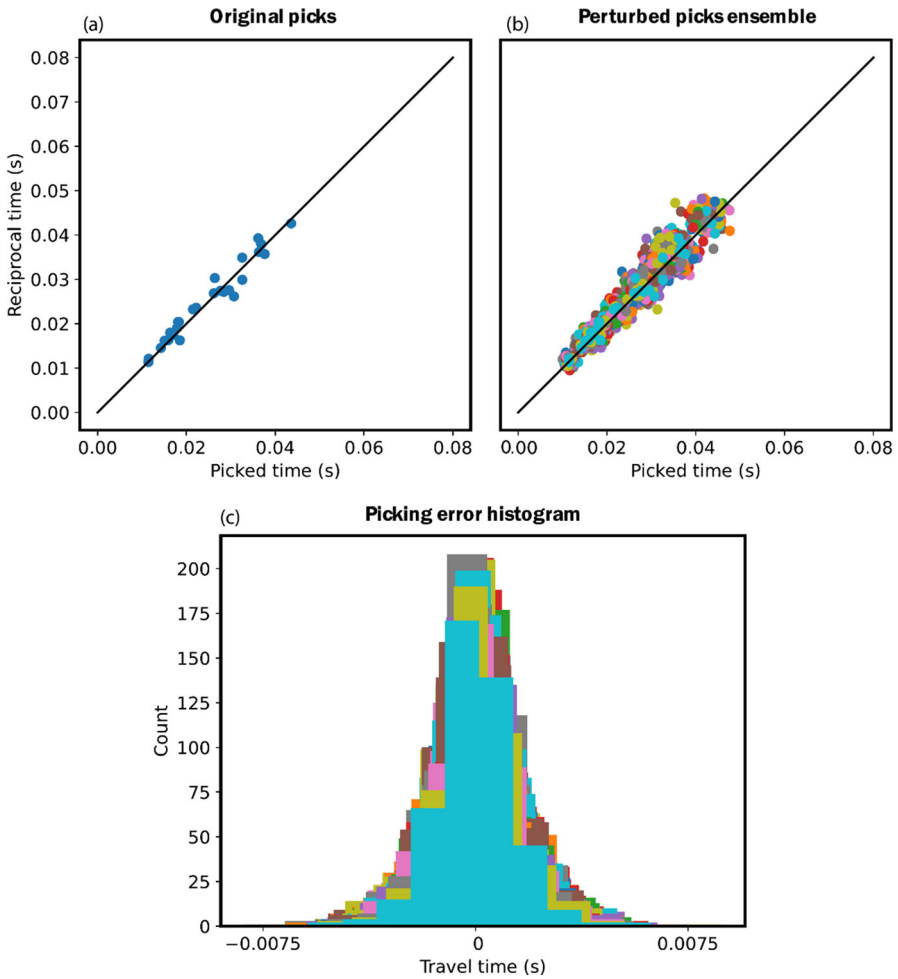
Fig. 7 Reciprocal travel times of the measured dataset at 25 available receiver locations (**a**). Reciprocal travel times of the perturbed travel time data for the ensemble of 100 realizations at the 25 receiver locations (2,500 values in total) where each color represents a different realization (**b**). Histogram of the perturbed travel times where each color represents a different realization (**c**)

3.3 Uncertainty in Both Initial Model and Data

In the previous sections, the uncertainty in the initial model and in the travel time data is investigated independently. In this section, the effect of the two sources of uncertainty on the final velocity model is studied by simultaneously perturbing both initial model and travel time data and running the inversion with the perturbed initial model and perturbed travel time data. The method is applied to all four transects for which initial model and picked arrival times for each transect are stochastically perturbed at the mid-uncertainty case. For each transect, 100 realizations of perturbed initial model
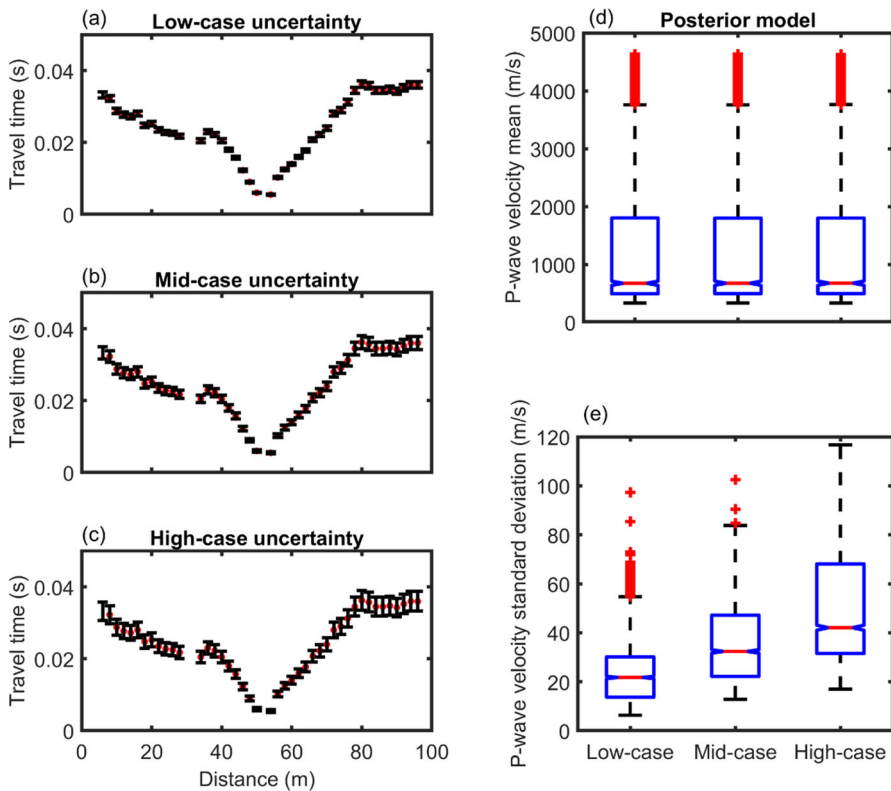
Fig. 8 Perturbed travel time picks with 95% CI (**a–c**) at low-, mid- and high-uncertainty cases for a source location at 50 m for PP8. Box plots for posterior model of P-wave velocity: mean (**d**) and standard deviation (**e**) of 100 realizations obtained by perturbing travel time picks

and data are generated and used as inputs for inversion, then the posterior ensemble of the inverted velocity models is obtained. The mean of the posterior P-wave velocity ensemble (Fig. 11), the mean of the posterior vertical velocity gradient ensemble (Fig. 12) and the standard deviation of the posterior P-wave velocity ensemble (Fig. 13) are studied.

The mean of the posterior ensemble of velocity models for PP8 (Fig. 11a) preserves similar structural patterns in velocity compared to the inverted model using a deterministic approach (Fig. 3b). Using the results obtained for PP8, several features can be identified. Below the topographic minimum at about 24 m in the horizontal distance, an approximately 3-m-thick layer ($V_p < 1{,}000$ m/s) overlies a much thicker layer ($V_p > 3{,}000$ m/s). The low-velocity layer becomes thicker as distance from the topographic minimum increases; hence, depth to the high-velocity layer increases below the hillslope at higher relative elevations (Fig. 11a). Below the topographic minimum, the value of the vertical velocity gradient ($\nabla V_p \sim 600$ m/s/m) is the highest across the profile (Fig. 12a). Likewise, high vertical velocity gradient values generally mark the transition zone from low-velocity layer to high-velocity layer. The highest standard
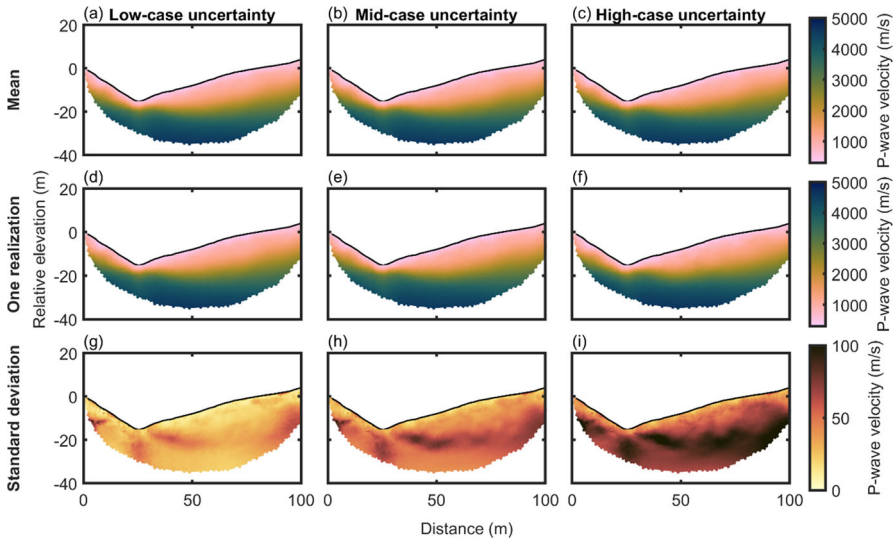
Fig. 9 Posterior model of P-wave velocity for PP8: mean of 100 realizations (**a–c**), one randomly selected realization (**d–f**), and standard deviation of 100 realizations (**g–i**) obtained by perturbing travel time picks at low-, mid- and high-uncertainty cases
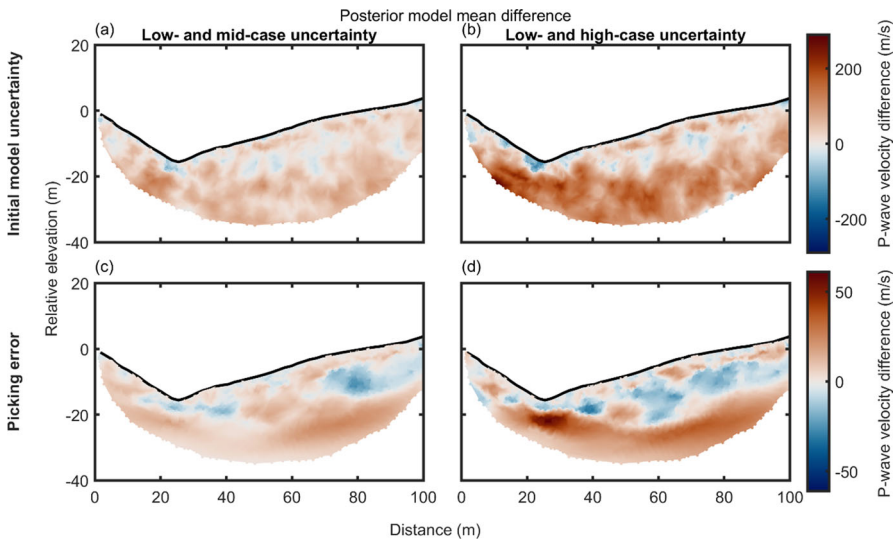

Fig. 10 Posterior model mean difference in low- and mid-uncertainty cases and in low- and high-uncertainty cases obtained by perturbing both the initial model (**a, b**) and travel time picks (**c, d**) for PP8
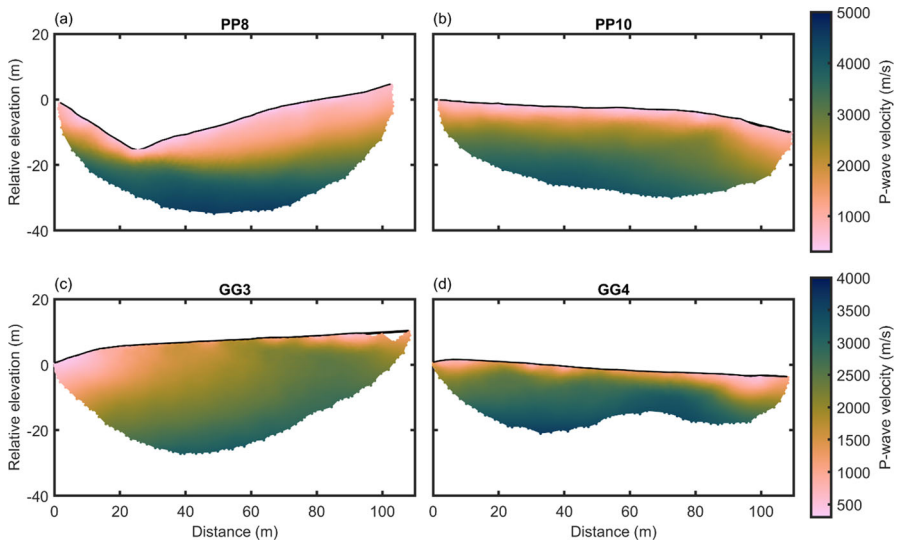
Fig. 11 Posterior model of P-wave velocity: mean of 100 realizations for PP8 (**a**), PP10 (**b**), GG3 (**c**) and GG4 (**d**) obtained by perturbing both the initial model and travel time data at mid-uncertainty case
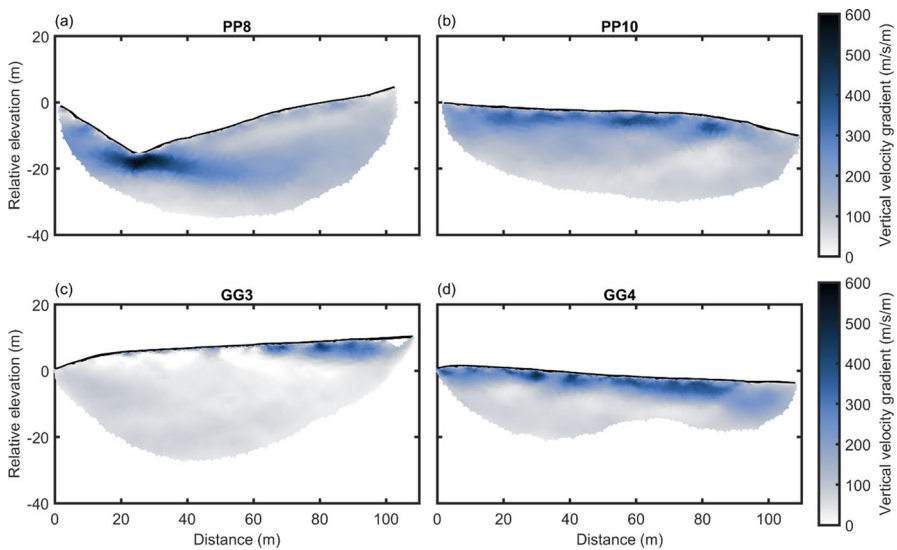

Fig. 12 Posterior model of P-wave vertical velocity gradient: mean of 100 realizations for PP8 (**a**), PP10 (**b**), GG3 (**c**) and GG4 (**d**) obtained by perturbing both the initial model and travel time data at mid-uncertainty case
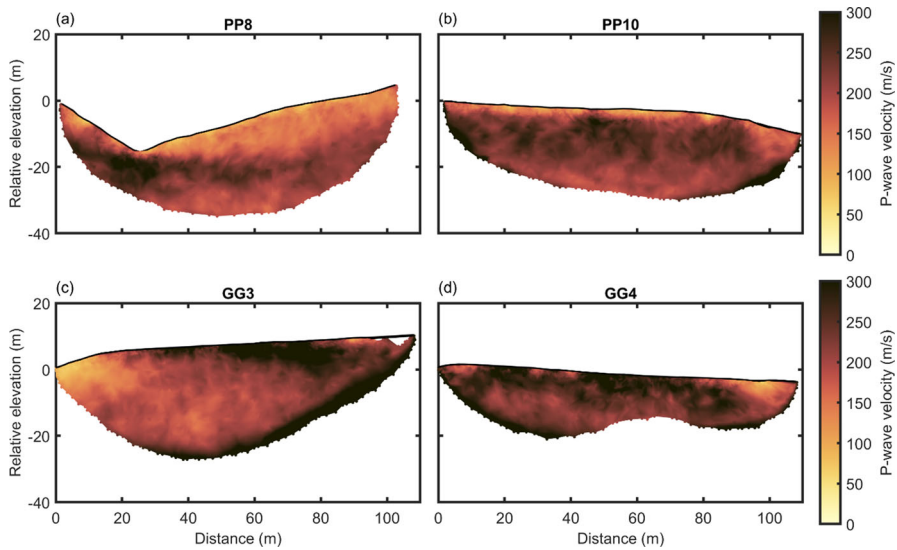
Fig. 13 Posterior model of P-wave velocity: standard deviation of 100 realizations for PP8 (**a**), PP10 (**b**), GG3 (**c**) and GG4 (**d**) obtained by perturbing both the initial model and travel time data at mid-uncertainty case

deviation ($\sigma_{V_p} \sim 300$ m/s) is below the topographic minimum, which corresponds to the structural pattern identified in the vertical velocity gradient that highlights the transition zone of low-velocity layer and high-velocity layer (Fig. 13a).

Unlike PP8 that features a stronger topographic relief, the other three transects (PP10, GG3 and GG4) features less variation in topography. In PP10, the thickness of the low-velocity layer ($V_p < 1,000$ m/s) is approximately constant along the transect and is generally less than 5 m (Fig. 11b). The high-velocity layer ($V_p > 3,000$ m/s) underneath the thinner low-velocity layer is generally thicker than the high-velocity layer of PP8. The interface between the low-velocity layer and the high-velocity layer is highlighted by the vertical velocity gradients with $\nabla V_p > 300$ m/s/m (Fig. 12b). The standard deviation increases beneath the transition zone of low-velocity layer and high-velocity layer (Fig. 13b). Although study sites at Pilot Peak and Government Gulch share similar sedimentary rock types, the underlying layer thicknesses, local lithology and porosity variations are different. In GG3, a high-velocity structure ($V_p \sim 2,500$ m/s) is observed near the end of line at about 2 m below the surface. A high-velocity zone with velocity ($V_p \sim 3,000$ m/s) is at about 20 m below the surface at the center of the line (Fig. 11c). The high-velocity structure observed near the end of line is related to the high vertical velocity gradient values ($\nabla V_p > 300$ m/s/m) (Fig. 12c). The standard deviation values are related to the velocity values (Fig. 13c). In GG4, the low-velocity layer ($V_p < 1,000$ m/s) is much thinner compared to other profiles. The transition zone of low-velocity layer and high-velocity layer is generally parallel to the topography (Fig. 11d). The transition from low to high velocity is highlighted by vertical velocity gradient with values higher than 300 m/s/m (Fig. 12d). The standard

deviation values generally increase along the velocity transition and along the DOI (Fig. 13d).

4 Discussion

While seismic refraction methods have become widely used in near-surface applications for estimating subsurface properties, the effects on the inverted tomographic velocity models of the different sources of errors remain unclear. This work proposes a stochastic method for quantifying uncertainty in the inverted velocity tomogram and demonstrates its application to field data. More specifically, this study investigates the effect of epistemic uncertainty in the initial model and aleatory uncertainty of the picking error on the inverted velocity models using a Monte Carlo-based approach. The result shows that both initial model and picking error contribute to the uncertainty in the velocity model, and that the initial model leads to larger uncertainty in the velocity models than picking error.

Previous studies demonstrate that the use of accurate and physically plausible initial model is effective in reducing the epistemic uncertainty in the inversion (Palmer 2012; Chen and Zelt 2016; Cai and Zelt 2022). This study investigates the effect of the uncertainty of the initial model on the predicted velocity model. By stochastically perturbing the initial model and travel time data using a Monte Carlo approach, the uncertainty in the predictive velocity model is quantified and the effect of the sources of uncertainty is studied individually and jointly. The set of initial models can be stochastically generated using geostatistical methods such as fast Fourier transform—moving average or probability field simulations (Grana et al. 2021). However, since the initial model is defined on a triangular grid, the application of traditional geostatistics method is challenging when the size of the triangles varies significantly (Zaytsev et al. 2016). Instead, spatially uncorrelated random noise is added to a subset of randomly selected locations within model grid and the values are interpolated on the full grid. This approach allows generating a set of initial models where the variability in the realizations depends on the standard deviation of the random noise. Preliminary tests show that the variability in the velocity models is consistent with the velocity ranges observed in near-surface geophysics boreholes (Flinchum et al. 2018a; Parsekian et al. 2021).

The aleatory uncertainty in the travel times is generally difficult to quantify. Although uncertainty in seismic refraction data which arises from measurement and processing errors can be quantified using the reciprocity principle, it often requires interpolation for traces that lack reciprocal measurements and therefore can be biased towards measurements with high reciprocal errors. Dangeard et al. (2018) proposed a method for estimate picking error by repeating the data processing multiple times, but their approach can be biased towards data being processed by the same operator and their manual repetition method becomes challenging for datasets that cover tens of kilometers in area. This study proposes a stochastic approach to quantify the uncertainty in the inverted model due to the errors in the travel time picking based on the assumption that picking error increases as a function of travel time. This assumption

might fail in cases where travel times are picked with minimum ambiguity given a high signal-to-noise ratio across the entire shot gather.

By comparing the independent effect of epistemic uncertainty due to local variability in the initial model and aleatoric variability in the picked travel time data on the posterior ensemble uncertainty, it is determined that epistemic uncertainty in the initial model has a larger effect on the posterior model uncertainty than aleatory variability in the data. This finding agrees with Palmer (2012) who demonstrates that minimizing epistemic uncertainty through the use of the most appropriate starting model is more important than minimizing aleatory variability. Palmer (2012) used field data imaging an ore body within a fractured volcanic and siltstone substrate in contrast to the field data from this study that was measured on interbedded limestones and sandstones, suggesting that the importance of the starting model over the data errors is not lithology-specific. In general, it is difficult to define an accurate starting model; however, this analysis shows that it is crucial to reduce the uncertainty in the initial model, for example using direct measurements from core samples and borehole log data, to obtain a more accurate and precise posterior model. Indeed, when a large dataset of direct measurements is available, it is generally possible to build a more accurate initial model using geostatistical interpolation or sampling methods (Grana et al. 2021). In these cases, the uncertainty in the initial model can be significantly reduced. Direct measurements are particularly useful in presence of low-quality geophysical data, as in these cases the uncertainty in the travel time data might have a larger effect on the velocity estimate than the uncertainty in the initial model. In practice though, this case is not very frequent due to the lack of borehole data for near-surface geophysics and the challenges in measuring velocities on unconsolidated core samples as well as the possibility of repeating the geophysical data acquisition in case of low-quality measurements.

The analysis of multiple seismic lines (Figs. 11, 12, 13) provides additional insights on the correlation between the posterior uncertainty, represented by the standard deviation of the velocity model, and other properties such as predicted velocity as well as depth (Fig. 14), ray coverage (Fig. 15) and vertical velocity gradient (Fig. 16). Generally, for PP and GG lines, the predicted velocity increases as a function of depth (Fig. 14), which agrees with velocity-depth models where deeper rocks are less porous and stiffer than shallower rocks with higher velocities (Mavko et al. 2020). At shallower depths where rocks are more porous, and softer and greater heterogeneity is expected, the predicted velocity increases rapidly as a function of depth, and high velocity gradient is observed; in contrast, at greater depths, the predicted velocity increases gradually and low velocity gradient is observed (Fig. 16). For the GG lines, the consolidated rock is observed to be shallow as a portion of the seismic line is almost on bare bedrock; hence, seismic rays are turning at shallower depth, and deeper rocks that are stiffer are not resolved. Indeed, the highest predicted velocity of GG lines (~ 3,500 m/s) is smaller that of PP lines (> 4,000 m/s), where stiffer rocks are at greater depth (Fig. 14).

Generally, for all lines, the posterior standard deviation increases as a function of the predicted velocity (Fig. 14). The increase is observed to be linear and rapid at shallower depths (< 5 m) for low predicted velocity values and stabilizes at some asymptotic value at greater depths (> 5 m) for high predicted velocity values. This
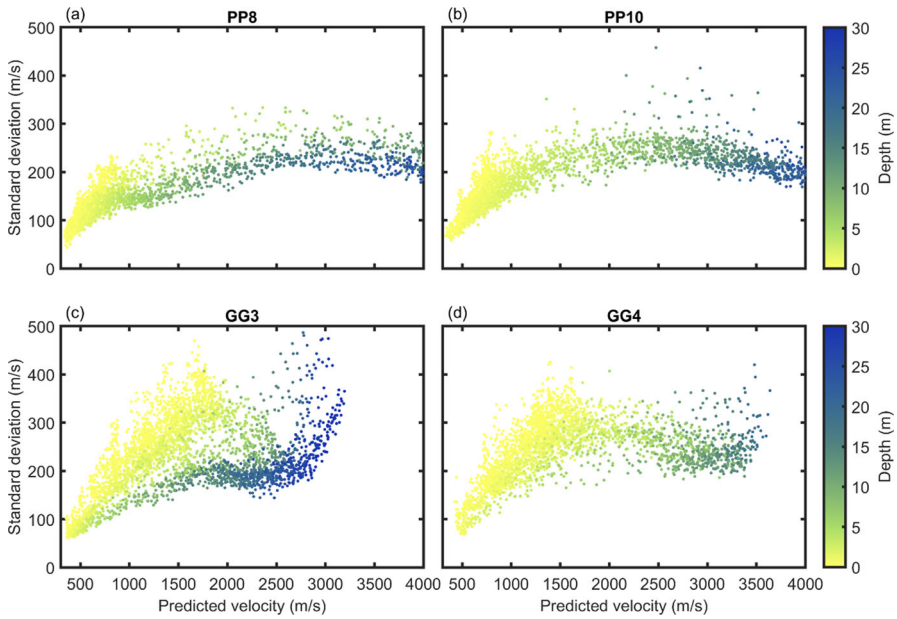
Fig. 14 Cross plot of posterior model standard deviation and mean of 100 realizations color-coded by depth for PP8 (**a**), PP10 (**b**), GG3 (**c**) and GG4 (**d**)
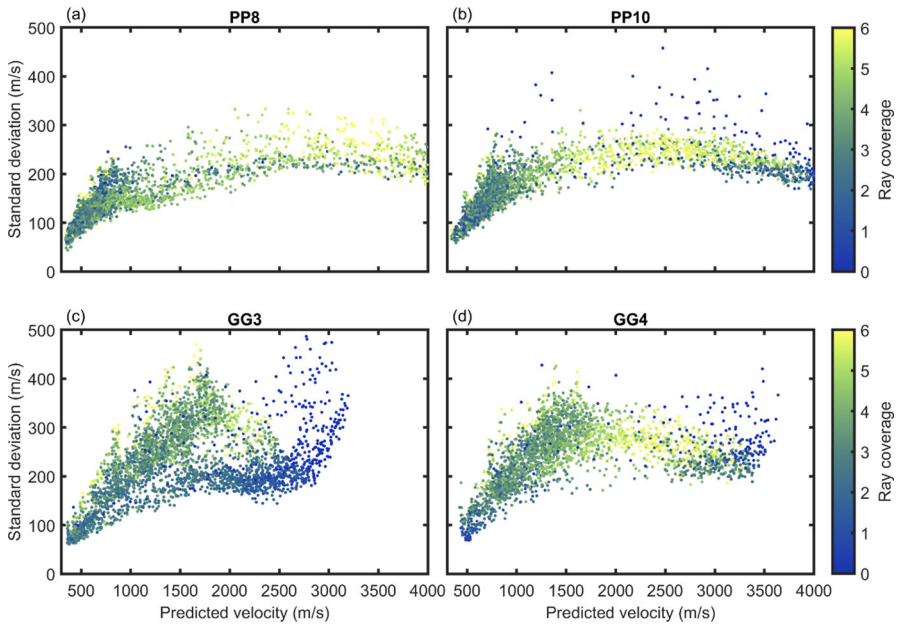

Fig. 15 Cross plot of posterior model standard deviation and mean of 100 realizations color-coded by ray coverage for PP8 (**a**), PP10 (**b**), GG3 (**c**) and GG4 (**d**)
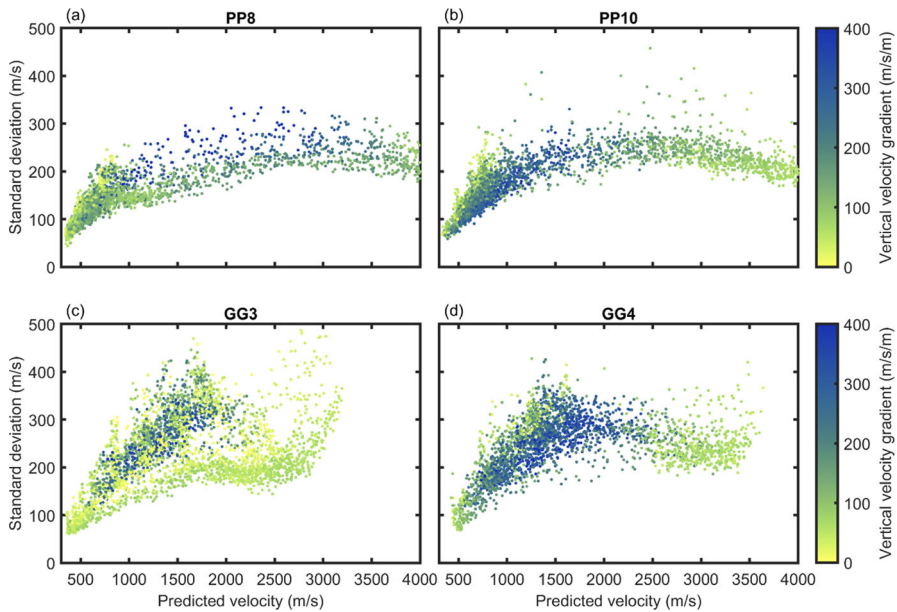
Fig. 16 Cross plot of posterior model standard deviation and mean of 100 realizations color-coded by vertical velocity gradient for PP8 (**a**), PP10 (**b**), GG3 (**c**) and GG4 (**d**)

pattern is consistent with the evidence that high velocity gradient is observed near the surface (Fig. 16) where high heterogeneity is present, and the predicted velocity has more variability and therefore uncertainty increases as a function of depth (Fig. 14). Furthermore, at greater depth where small velocity gradient is observed (Fig. 16) and less heterogeneity in the rocks is expected, velocity for such stiffer rocks is predicted with less local variability, and therefore the associated uncertainty in the prediction is almost constant as the standard deviation stabilizes at some asymptotic value (Fig. 14). Although for GG lines, standard deviation also appears to increase as a function of the predicted velocity even at greater depth (Fig. 14c, d), it is reasonable to speculate that this is due to insufficient ray coverage near the DOI that causes uncertainty to increase with the predicted velocity (Fig. 15c, d). In general, for areas with high velocity gradients, high values of standard deviation are observed (Fig. 16). For example, at the transition from low-velocity to high-velocity layers with the predicted velocity in the range of 700–2,000 m/s, which may indicate a transition from high-porosity soft rocks to low-porosity stiff rocks (Flinchum et al. 2018a; Holbrook et al. 2019), the observed standard deviation increases with the predicted velocity due to higher local variability in the prediction (Fig. 16) and may be attributed to the smoothing constraint enforced in the inversion.

Overall, similar patterns of spatial variation in the obtained standard deviation are observed among all lines; however, a bimodal trend in GG3 is observed (Figs. 14c, 15c, 16c). The bimodal trend as observed in GG3 is most likely due to large spatial heterogeneity along the surface (Figs. 11c, 12c) that causes variation in both the

predicted velocity values and velocity gradient values. In GG3, a zone of high velocity and sharp velocity change is observed at $X = 60$ m and beyond (Figs. 11c, 12c) and likely corresponds to the linear trend with a higher gradient (Fig. 16c), whereas the other zone with lower velocity and no significant velocity change observed at less than $X = 60$ m (Figs. 11c, 12c) likely corresponds to the linear trend with a smaller gradient (Fig. 16c).

5 Conclusions

A stochastic methodology is presented for quantifying uncertainty in seismic tomographic inversion that arises from epistemic uncertainty and aleatory variability in data. By stochastically perturbing the initial model and travel time picks and generating an ensemble of realizations using a Monte Carlo approach, the effects of epistemic uncertainty and aleatory variability in data on the inverted velocity model are investigated. By combining both sources of errors and studying the effect on the posterior model uncertainty, some general conclusions are drawn: (i) uncertainty generally increases rapidly as a function of the predicted velocity and depth in the near subsurface (i.e., high-porosity soft rocks) and becomes approximately constant in the deeper part (i.e., low-porosity stiff rocks); (ii) uncertainty increases in areas with insufficient ray coverage; (iii) uncertainty is generally higher in areas with higher values of velocity gradient and therefore higher degree of heterogeneity (e.g., transition from high-porosity soft rocks to low-porosity stiff rocks) and is lower in areas with lower values of velocity gradient and therefore less heterogeneity (e.g., low-porosity stiff rocks); (iv) uncertainty might have more than one trend as a function of the predicted velocity if large lateral heterogeneity in the subsurface is observed. As this study specifically investigates the effect of the two sources of errors on the uncertainty of the inversion result, there are other possible sources of errors that might drive uncertainty in the inversion result and remain to be further investigated, for example, errors in the measured topography, choice of regularization parameter, grid shape, and grid size. The proposed approach can be extended to seismic refraction data collected at any field sites with variable regional geology for the quantification of epistemic uncertainty (i.e., the inherent sensitivity of inversion parameters such as the initial model) and aleatory uncertainty in data (i.e., the variability in picking error). Furthermore, the proposed method can also be extended to other types of geophysical data, such electric data, and to other rock and fluid properties, such as porosity and water saturation.

Data Availability Data associated with this research are available and can be access via the following: https://www.hydroshare.org/resource/80467506c1134bd8a66bb3f518dd72ab/.

Declarations

Conflict of interest The authors declare that they have no financial nor non-financial conflicts of interest related to this work.

References

Ackerer J, Steefel C, Liu F, Bart R, Safeeq M, O'Green A, Hunsaker C, Bales R (2020) Determining how critical zone structure constrains hydrogeochemical behavior of watersheds: learning from an elevation gradient in California's Sierra Nevada. Front Water 2:23

Anderson SP, von Blanckenburg F, White F (2005) Physical and chemical controls on the critical zone. Elements 3(5):315–319

Aster RC, Borchers B, Thurber CH (2018) Parameter estimation and inverse problems. Elsevier, Amsterdam

Bales RC, Dietrich WE (2020) Linking critical zone water storage and ecosystems. Eos. https://doi.org/10.1029/2020EO150459

Befus KM, Sheehan AF, Leopold M, Anderson SP, Anderson RS (2011) Seismic constraints on critical zone architecture, Boulder Creek Watershed, Front Range, Colorado. Vadose Zone J 10:915–927

Borcherdt RD, Healy JH (1968) A method for estimating the uncertainty of seismic velocities measured by refraction techniques. Bull Seismol Soc Am 58(6):1769–1790

Brantley SL, Goldhaber MB, Ragnarsdottir KV (2007) Crossing disciplines and scales to understand the critical zone. Elements 3(5):307–314

Cai A, Zelt CA (2022) Early arrival waveform inversion using data uncertainties and matching filters with application to near-surface seismic refraction data. Geophysics 87(6):465–486

Callahan RP, Riebe CS, Pasquet S, Ferrier KL, Grana D, Sklar LS, Taylor NJ, Flinchum BA, Hayes JL, Carr BJ, Hartsough PC, O'Geen AT, Holbrook WS (2020) Subsurface weathering revealed in hillslope-integrated porosity distributions. Geophys Res Lett 47(15):e2020GL088322

Callahan RP, Riebe CS, Sklar LS, Pasquet S, Ferrier KL, Hahm WJ, Taylor NJ, Grana D, Flinchum BA, Hayes JL, Holbrook WS (2022) Forest vulnerability to drought controlled by bedrock composition. Nat Geosci 15:714–719

Chen J, Zelt CA (2016) Application of frequency-dependent traveltime tomography and full waveform inversion to realistic near-surface seismic refraction data. J Environ Eng Geophys 21(1):1–11

Chen J, Hubbard SS, Gaines D, Korneev V, Baker G, Watson D (2010) Stochastic estimation of aquifer geometry using seismic refraction data with borehole depth constraints. Water Resour Res 46:W11539

Crameri F (2021) Scientific colour maps (7.0.1). Zenodo. https://doi.org/10.5281/zenodo.5501399

Dangeard M, Bodet L, Pasquet S, Thiesson J, Guerin R, Jougnot D, Longuevergne L (2018) Estimating picking errors in near-surface seismic data to enable their time-lapse interpretation of hydrosystems. Near Surf Geophys 16:613–625

Dehoop AT (1966) An elastodynamic reciprocity theorem for linear, viscoelastic media. Appl Sci Res 16:39–45

Dijkstra EW (1959) A note on two problems in connexion with graphs. Numer Math 1:269–271

Efron B (1979) Bootstrap methods: another look at the jackknife. Anal Stat 7(1):1–26

Efron B (1982) The Jackknife, the bootstrap and other resampling plans. SIAM

Flinchum BA, Holbrook WS, Grana D, Parsekian AD, Carr BJ, Hayes JL, Jiao J (2018a) Estimating the water holding capacity of the critical zone using near-surface geophysics. Hydrol Process 32(22):3308–3326

Flinchum BA, Holbrook WS, Rempe D, Moon S, Riebe CS, Carr BJ, Hayes JL, St. Clair J, Peters MP (2018b) Critical zone structure under a granite ridge inferred from drilling and three-dimensional seismic refraction data. J Geophys Res Earth Surf 123(6):1317–1343

Flinchum BA, Holbrook WS, Carr BJ (2022) What do P-wave velocities tell us about the critical zone? Front Water 3:772185. https://doi.org/10.3389/frwa.2021.772185

Gase AC, Bradford JH, Brand BD (2018) Estimation of porosity and water saturation in dual-porosity pyroclastic deposits from joint analysis of compression, shear, and electromagnetic velocities. Geophysics 83(3):ID1–ID11

Grana D, Mukerji T, Doyen P (2021) Seismic reservoir modelling. Wiley, Hoboken

Grana D, Parsekian AD, Flinchum BA, Callahan RP, Smeltz NY, Li A, Hayes JL, Carr BJ, Singha K, Riebe CS, Holbrook WS (2022) Geostatistical rock physics inversion for predicting the spatial distribution of porosity and saturation in the critical zone. Math Geosci 54:1315–1345

Grouveia WP, Scales JA (1998) Bayesian seismic waveform inversion: parameter estimation and uncertainty analysis. J Geophys Res 103(B2):2759–2779

Gu X, Mavko G, Ma L, Oakley D, Accardo N, Carr BJ, Nyblade AA, Brantley SL (2020) Seismic refraction tracks porosity generation and possible CO_2 production at depth under a headwater catchment. Proc Natl Acad Sci 117(32):18991–18997

Hahm WJ, Rempe DM, Dralle DN, Dawson TE, Lovill SM, Bryk AB, Bish DL, Schieber J, Dietrich WE (2019) Lithologically controlled subsurface critical zone thickness and water storage capacity determine regional plant community composition. Water Resour Res 55(4):3028–3055

Hayes JL, Riebe CS, Holbrook WS, Flinchum BA, Hartsough PC (2019) Porosity production in weathered rock: Where volumetric strain dominates over chemical mass loss. Sci Adv 5(9):eaao0834

Holbrook WS, Marcon V, Bacon AR, Brantley SL, Carr BJ, Flinchum BA, Richter DD, Riebe CS (2019) Links between physical and chemical weathering inferred from a 65-m-deep borehole through Earth's critical zone. Sci Rep 9:4495. https://doi.org/10.1038/s41598-019-40819-9

Holbrook WS RCS, Elwaseif ML, Hayes JL, Basler-Reeder KL, Harry DL, Malazian K, Dosseto AC, Hartsough P, Hopmans J (2014) Geophysical constraints on deep weathering and water storage potential in the Southern Sierra critical zone Observatory. Earth Surf Proc Land 39(3):366–380

Huang MH, Hudson-Rasmussen B, Burdick S, Lekic V, Nelson MD, Fauria KE, Schmerr N (2021) Bayesian seismic refraction inversion for critical zone science and near-surface applications. Geochem Geophys Geosyst 22(5):e2020GC009172

Huntoon PW, Lundy DA (1979) Fracture-controlled ground-water circulation and well siting in the vicinity of Laramie, Wyoming. Ground Water 17(5):463–469

Knight R, Endres A (2005) An introduction to rock physics principles for near-surface geophysics. In: Butler DK (ed) Near-surface geophysics. Society of Exploration Geophysicists, pp 31–70

Leopold M, Volkel J, Huber J, Dethier D (2013) Subsurface architecture of the Boulder Creek Critical Zone Observatory from electrical resistivity tomography. Earth Surf Proc Land 38:1417–1431

Liu C, Stock JM (1993) Quantitative determination of uncertainties in seismic refraction processing. Geophysics 58(4):553–563

Marciniak A, Stan-Kleczek I, Idziak A, Majdanski M (2019) Uncertainty based multi-step seismic analysis for near-surface imaging. Open Geosci 11:727–737

Mavko G, Mukerji T, Dvorkin J (2020) The rock physics handbook. Cambridge University Press, Cambridge

McCormick EL, Dralle DN, Hahm WJ, Tune AK, Schmidt LM, Chadwick KD, Rempe DM (2021) Widespread woody plant use of water stored in bedrock. Nature 597(7875):225–229

Moravec BG, White AM, Root RA, Sanchez A, Olshansky Y, Paras BK, Carr B, McIntosh J, Pelletier JD, Rasmussen C, Holbrook WS, Chorover J (2020) Resolving deep critical zone architecture in complex volcanic terrain. J Geophys Res Earth Surf 125:e2019JF005189. https://doi.org/10.1029/2019JF005189

Moysey S, Singha K, Knight R (2005) A framework for inferring field-scale rock physics relationships through numerical simulation. Geophys Res Lett 32(8):L08304

Palmer D (2012) Uncertainty in near-surface refraction inversion. ASEG Ext Abstr 1:1–4

Parsekian AD, Singha K, Minsley BJ, Holbrook WS, Slater L (2015) Multiscale geophysical imaging of the critical zone. Rev Geophys 53:1–26

Parsekian AD, Grana D, Neves F, Pleasants MS, Seyfried M, Moravec BG, Chorover J, Moraes A, Smeltz N, Westenhoff JN, Kelleners T (2021) Hydrogeophysical comparison of hillslope critical zone architecture for different geologic substrates. Geophysics 86(3):1–84

Parsekian AD (2022) Laramie range summer 2022 environmental geophysics. HydroShare. http://www.hydroshare.org/resource/80467506c1134bd8a66bb3f518dd72ab

Prakoso S, Permadi P, Winardhi S, Marhaendrajana T (2018) Dependence of critical porosity on pore geometry and pore structure and its use in estimating porosity and permeability. J Pet Explor Prod Technol 8:431–444

Rawlinson N, Fichtner A, Sambridge M, Young MK (2014) Seismic tomography and the assessment of uncertainty. Adv Geophys 55:1–76

Rempe DM, Dietrich WE (2018) Direct observations of rock moisture, a hidden component of the hydrologic cycle. Proc Natl Acad Sci 115(11):2664–2669. https://doi.org/10.1073/pnas.1800141115

Riebe CS, Hahm WJ, Brantley SL (2017) Controls on deep critical zone architecture: a historical review and four testable hypotheses. Earth Surf Proc Land 42:128–156

Riebe CS, Callahan RP, Granke SBM, Carr BJ, Hayes JL, Schell MS, Sklar LS (2021) Anisovolumetric weathering in granitic saprolite controlled by climate and erosion rate. Geology 49(5):551–555

Robinson DA, Binley A, Crook N, Day-Lewis FD, Ferré T, Grauch V, Knight R, Knoll K, Lakshmi V, Miller R, Nyquist J (2008) Advancing process-based watershed hydrological research using near-surface geophysics: a vision for, and review of, electrical and magnetic geophysical methods. Hydrol Process 18:3604–3635

Rücker C, Günther T, Wagner FM (2017) pyGIMLi: An open-source library for modelling and inversion in geophysics. Comput Geosci 109:106–123

Schnaidt S, Heinson G (2015) Bootstrap resampling as a tool for uncertainty analysis in 2-D magnetotelluric inversion modelling. Geophys J Int 203:92–106

Singha K, Moysey S (2006) Accounting for spatially variable resolution in electrical resistivity tomography through field-scale rock-physics relations. Geophysics 71(4):A25–A28

St. Clair J, Moon S, Holbrook WS, Perron JT, Riebe CS, Martel SJ, Carr B, Harman C, Singha K, Richter D (2015) Geophysical imaging reveals topographic stress control of bedrock weathering. Science 350:534–538

Steinhart JS, Meyer RP (1961) Minimum statistical uncertainty of seismic refraction profile. Geophysics 26(5):574–587

Tarantola A (2005) Inverse problem theory and methods for model parameter estimation. SIAM

White A, Moravec B, McIntosh J, Olshansky Y, Paras B, Sanchez RA, Ferré T, Meixner T, Chorover J (2019) Distinct stores and the routing of water in the deep critical zone of a snow-dominated volcanic catchment. Hydrol Earth Syst Sci 23:4661–4683

Zaytsev V, Biver P, Wackernagel H, Allard D (2016) Change-of-support models on irregular grids for geostatistical simulation. Math Geosci 48(4):353–369. https://doi.org/10.1007/s11004-015-9614-x

Zelt CA, Chen J (2016) Frequency-dependent traveltime tomography for near-surface seismic refraction data. Geophys J Int 207:72–88